

## Source Parameters of the $M_w$ 5.8 Fin (South of Iran) Earthquake of March 25, 2006

*S. Ashkpour Motlagh and M. Mostafazadeh*

International Institute of Earthquake Engineering and Seismology (IIEES) Tehran, Iran

**Abstract:** Teleseismic body waveform modeling of the far-field  $P$ - and  $SH$ -waveforms and spectral analysis of  $P$ -waves are used to determine the source parameters of the March 25, 2006 Fin earthquake ( $m_b$  5.7). Its epicenter is located at the South of Iran in Hormozgan Province. The waveform modeling results show the earthquake was caused by a thrust motion on a NW-SE striking fault with parameters: Fault plane (strike=308°, dip = 30° and the rake of 95°) and auxiliary plane (strike = 113°, dip = 60°, rake = 100°), depth of 17 km and  $M_0$  of 6.728E17 N.m. The spectral analysis of the far-field  $P$ -wave pulses resulted in a fault length  $L \sim 17$  km, stress drop  $\Delta\sigma \sim 2.88$  bars and average displacement  $u \sim 9.5$  cm. In this study, the variant models to determine the source dimension were examined and found that the Madariaga model is more reliable than the other models and consequently, usable to estimate the source parameters.

**Key words:** Waveform modeling . spectral analysis . source parameters . Fin . Iran

### INTRODUCTION

On March 25, 2006 at 07:28:57.66 GMT (10:58:57.66 Local time), an earthquake of  $m_b$  5.7 occurred in the Hormozgan Province (South of Iran), 59 km NW of Bandar-e Abbas and 8 km SSW of Fin (Fig. 1); its epicenter was located at 27.575°N, 55.762°E. This event was followed by 10 earthquakes with  $m_b$  4.4-5.5 during 9 hours in a region of 24×44km<sup>2</sup> area (Fig. 2 and Table 1), while six of them were aligned sub parallel of High Zagros Fault (HZF) system. Despite its moderate magnitude, no damage was reported caused by this earthquake which may represent a damping cover on basement in this area such as salt plug.

The aim of this research is to investigate the source parameters of the March 25, 2006 Fin earthquake in details. So, we used teleseismic long period data from Global Seismograph Network (GSN). The focal mechanism and related parameters were determined by using the teleseismic waveform modeling. Furthermore, the average seismic moment, fault length, stress drop and displacement across the ruptured area were determined from the far-field displacement spectra of the main shock.

### TECTONIC SETTING

The active deformation in Iran is caused by Northward motion of Arabian plate with respect to Eurasia (Fig. 1). Approximately, half of the ~25 mm yr<sup>-1</sup> of Arabia-Eurasia shortening at latitude 60° E is taken up in the Zagros Mountains [1, 2].

The Zagros Mountains are situated on the deformed northern margin of the Arabia continental plate. The boundary between the Arabian and Iranian plates lies along the Zagros suture (Fig. 1). Folds within the Zagros contain one of the largest global reserves of hydrocarbons [3]. Seismic activity is widespread by many destructive earthquakes [4]. However, co-seismic fault slip at depth does not usually propagate to the Earth's surface in the Zagros, presumably because it is decoupled by the numerous evaporitic deposits in the ~10 km-thick Phanerozoic sedimentary sections [4, 5].

The Zagros Mountains are subdivided into the High Zagros and simply folded zones on the basis of topography, exposed stratigraphy and seismicity [5, 6]. The southern margin of the High Zagros lies along the High Zagros Fault (Fig. 1), which is usually the southern limit of exposure of Paleozoic rocks [5]. Most of the present-day deformation were determined by GPS [1, 2] and seismicity (e.g. Fig. 1) occurs in the simply folded zone (Fig. 1), in which shortening within young sedimentary rocks is accommodated as folding along broad whale-back anticlines. There is no seismic evidence for a low-angle reverse detachment beneath the Zagros and shortening at basement depth (>~ 10 km) is instead taken up by distributed high-angle reverse faulting [5]. The basement faults may be reactivated normal faults inherited by the rifted Tethyan margin of Arabia [5, 7-9]; but there is no conclusive evidence for this. Slip on basement faults does not rich the Earth's surface as it is decoupled from folding within sedimentary layers by thick evaporate deposits that occur at several levels within the Phanerozoic section, most importantly at the base, in the infra-Cambrian

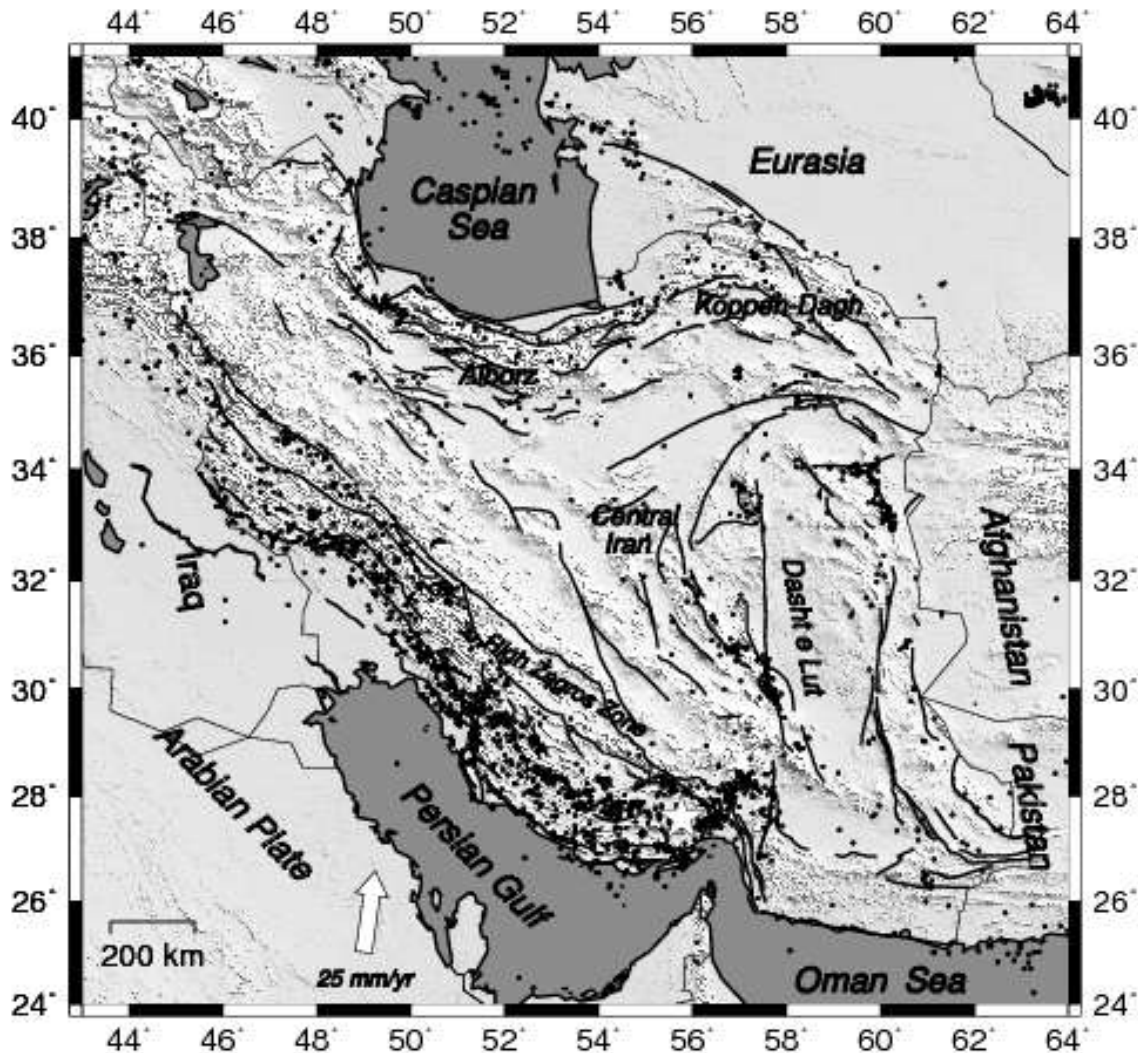


Fig. 1: A typical map of Iran which shows the major fault zones and geographical regions. The arrow with 25 mm/yr rate represents Arabia-Eurasia plate convergence [2]. Arabia-Eurasia convergence occurs in the Zagros, the Alborz, Kopeh Dagh and possibly in central Iran by the rotation of strike-slip faults. Right lateral shear between central Iran and Afghanistan is taken up on N-S right-lateral faults of the Gowk-Nayband and Sistan suture zone systems, which surround the Dasht-e-Lut. The Fin earthquake location is marked by a star, which is located in the southeastern end of Zagros. The small circles show the epicenters on recent Engdahl's catalogue (2007)

Hormoz Salt Formation. But it seems, there is another mechanism for deformation in southeastern of Zagros which is a collision zone and the basement motion has significant role to do it. Most of the earthquakes which occurred in southeastern edge of Zagros have depths of  $\approx 15$  km with low angle thrust motion on NW-SE striking faults without surface rupture.

### EARTHQUAKES

Although the study area is located in a high seismicity and complex zone and the seismicity maps

show dense epicenters of instrumental events (Fig. 1 and 2), there is no historical evidence of destructive earthquake [10]. Fin main-shock was followed by 11 earthquakes in which most of them occurred in the same day. They clustered in depths of  $>12$  km and their epicenters aligned sub parallel of High Zagros fault (Fig. 2). This alignment may be points to existence of a hidden fault at the basement with NW-SE strike. Table 1 represents the focal mechanisms and depth of March 25, 2006 Fin main-and after-shocks and was obtained by Harvard CMT solutions and waveform-modeling in this study.

Table 1: Source parameters of recent earthquakes in study area. Epicenters, Magnitudes ( $m_b$  and  $M_s$ ) and origin time are from Engdahl's (2007). Seismic moment ( $M_0$ ) is in units of  $10^{17}$  N.m. The last column gives the earthquake source parameters on each line: from body wave modeling in this paper (T) or from the CMT solutions by Harvard (H)

Time	Lat	Long	Depth	$m_b$	$M_s$	$M_w$	$M_0$	Strike	Dip	Rake	R
07:28:57.66	27.56	55.64	17	5.7	5.5	5.85	6.73	308	30	95	T
07:29:1.2	27.43	55.60	14	5.7	5.5	5.9	7.80	269	28	83	H
09:55:16.9	27.48	55.68	12	5.3	4.9	5.5	2.14	276	35	89	H
10:00:38.70	27.41	55.66	12	5.5	-	5.2	0.81	267	30	70	H
11:03:00.70	27.53	55.62	12	5.0	-	5.0	0.36	261	33	59	H
12:13:46.90	27.44	55.36	19	4.9	3.9	4.9	0.27	256	34	57	H

Teleseismic waveform modeling

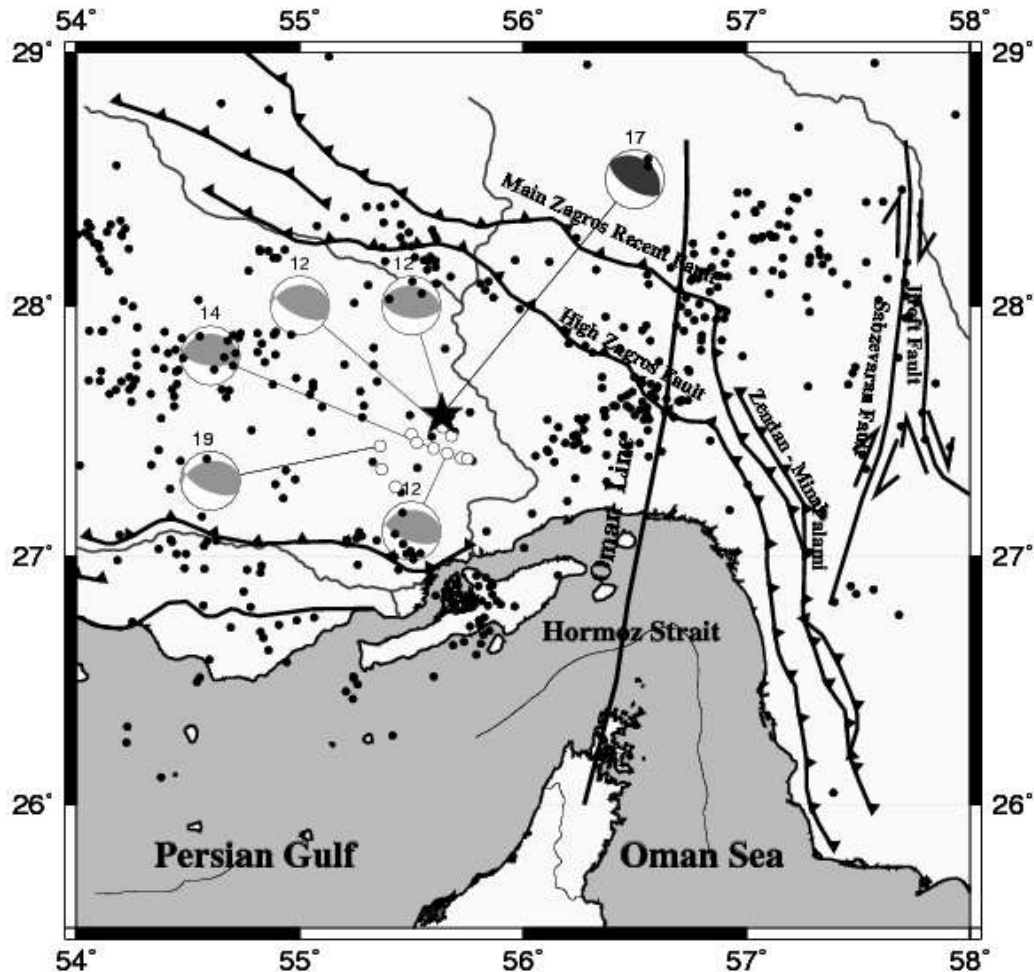


Fig. 2: Tectonic map of the study area and adjacent regions, in which the main faults were reported from IIEES reports. Beach balls show distribution and earthquake focal mechanisms of instrumentally recorded events. Mechanisms constrained by body wave inversion in this study are in light black and light gray beach balls are Harvard CMT solutions ( $M_w = 4.9$ ) of main- and after-shocks of the Fin earthquake. The small dark circles show the epicenters on recent Engdahl's catalogue (2007), the white circles show the epicenters of Fin earthquake aftershocks and the epicenter of main shock is shown by a star. Oman Line is assumed a border line between Zagros and Makran subduction zone, as a collision zone

### METHODOLOGY AND APPLICATION

The technique of body-waveform modeling, described in details by Nábélek [11] and McCaffery *et al.* [12], was used to calculate the focal mechanism of the Fin earthquake that occurred on March 25, 2006. The employed data consist of *P*- and *S*-waveforms from stations of Global Seismograph Network (GSN). All waveforms have a sampling frequency of 1 Hz and were recorded at epicentral distances ranging from 30° to 90° as teleseismic distance. At teleseismic distance the *P*- and *S*-waves arrive clearly separated in time from each other, as well as other seismic phases and therefore can be analyzed independently. The wave forming packets of teleseismic *P*- and *S*-waves are characterized by essentially constant ray parameters and involve all direct, reflected and converted waves which propagate through the earth's mantle along the path of minimum travel times as *P*- or *S*-wave, respectively.

We used the MT5 version [13] of McCaffery and Abers [14] algorithm to invert *P*- and *SH*-waveform data in order to obtain the strike, dip, rake, centroid depth, seismic moment and source time function of the examined event. The methodology assumes that the source (with  $M_s = 6.6$ ) can be represented as a point source (the centroid) in space, although not in time. The time history of the displacement of the fault is represented by a source time function made up by a series of overlapping isosceles triangles, which numbers and duration are defined by the user. The inversion routine yields amplitudes were corrected for

each triangular shape. Amplitudes were corrected for the geometrical spreading, the epicentral distance [15] and the attenuation using Futterman's [16] operator with  $t^* = 1$  s and 4 s for *P*-waves for *SH*-waves respectively. The inversion adjusts the relative amplitudes of the source time function elements, the centroid depth, the seismic moment and the source orientation (strike, dip and rake) to minimize the misfit between observed and synthetic seismograms. We refer to this solution as the *minimum misfit solution*. The covariance matrix associated with the *minimum misfit solution* usually underestimates the true uncertainties associated with the source parameters. To find more realistic uncertainties, we followed the methodology of McCaffery and Nábélek [17] and Molnar and Lyon-Caen [18] by fixing some of the source parameters at values close to, but different from those of the *minimum misfit solution* and allowing all other parameters to vary during the inversion. The errors are determined by visual examination when the match of the observed to synthetic seismograms significantly deteriorates. Synthetics were generated for a point source buried in a half-space.

### INVERSION RESULTS

The focal mechanism and centroid depth of the March 25, 2006 earthquake were computed by inverting 23 *P*- and 9 *SH*-Long-Period waves with good azimuthally coverage (Fig. 3). The results are shown in Fig. 4, 5 and Table 1. The solution indicates thrust

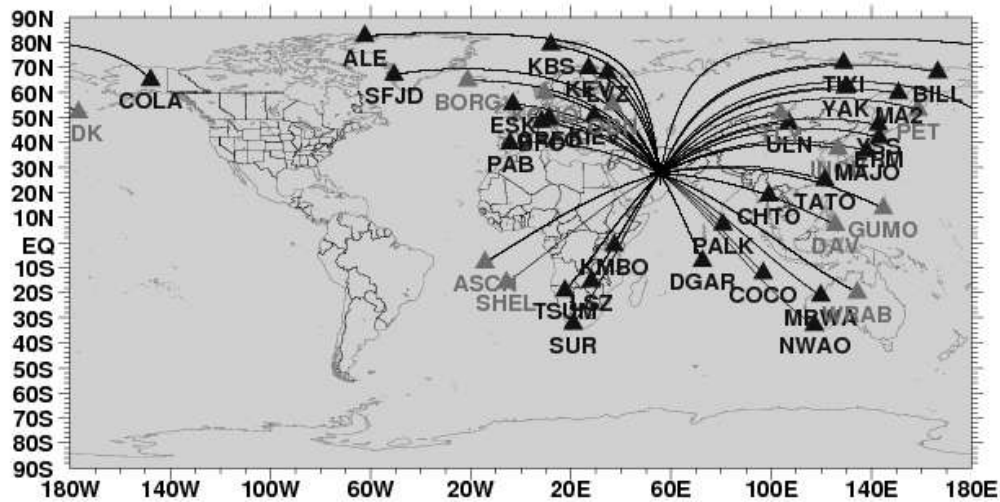


Fig. 3: Map of Incorporated Research Institutions for Seismology (IRIS) stations ( $\Delta=30^{\circ}$ - $90^{\circ}$ ) which has recorded the seismograms of Fin earthquake. The triangles indicate the station location and alphabetic marks indicate the station code. The black triangles are the stations with good signal to noise that we used in this study and the grays are poor signal to noise ratio. This figure shows the appropriated azimuthally distribution with the gap less than 50°

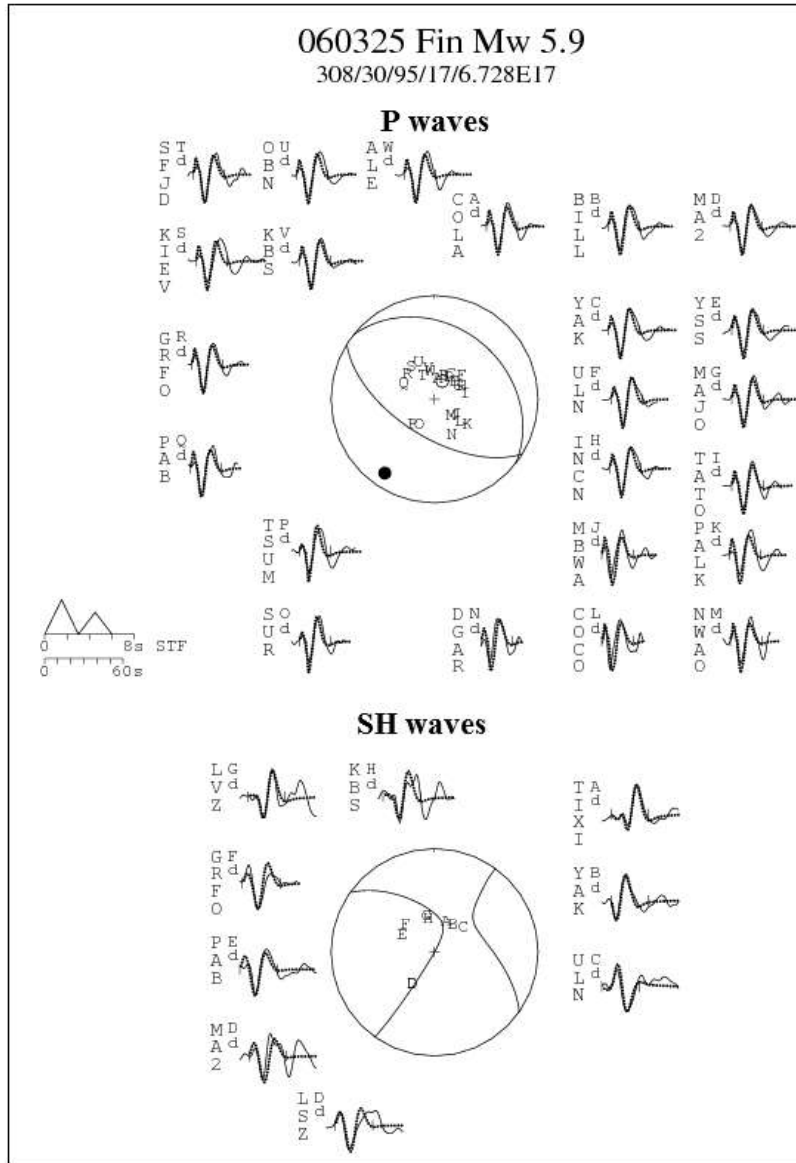


Fig. 4: Minimum misfit solution for the 25 March 2006 earthquake in Fin area (Table 2) showing *P* (top) and *SH* (bottom) observed (solid) and synthetic (dotted) waveforms. Waveforms for each station are arranged azimuthally around the focal spheres. Station positions on focal spheres are identified by capital letters and arranged clockwise starting from north. STF is the source time function. Vertical ticks on the seismograms indicate the inversion window. Numbers beneath the header line are strike, dip, rake, centroid depth (km) and scalar moment (N.m). Stations were weighted according to azimuthally density and then, S seismograms weights were halved to compensate for their larger amplitudes. *P* and *T* axes are represented by a black and white dot. We carried out the velocity structure in this study a single layer with 10 km thick,  $V_p = 6 \text{ km.s}^{-1}$ ,  $V_s = 3.45 \text{ km.s}^{-1}$  and  $\rho = 2.75 \text{ gr.cm}^{-3}$  over a half space of  $V_p = 6.8 \text{ km.s}^{-1}$  and  $V_s = 3.85 \text{ km.s}^{-1}$  and  $\rho = 2.91 \text{ gr.cm}^{-3}$  over a half space of  $V_p = 6.5 \text{ km.s}^{-1}$ ,  $V_s = 3.7 \text{ km.s}^{-1}$  and  $\rho = 2.85 \text{ g.cm}^{-3}$

motion on a fault dipping  $30^\circ (\pm 2^\circ)$  NNE, with a strike of  $308^\circ (-8^\circ/+10^\circ)$ , a rake of  $95^\circ (\pm 10^\circ)$  a hypocentral depth of 17 km (-3 / +2 km), a source time function with a duration of 6 seconds while 95% of the energy was abruptly released within the first 4.5 sec and a

scalar moment of  $6.728 \times 10^{17}$  N.m. The focal depth which we deduced from waveform modeling is good agreement with depth of 15.8 km and was reported by International Institute of Earthquake Engineering and Seismology (IIEES) based on regional data. Following

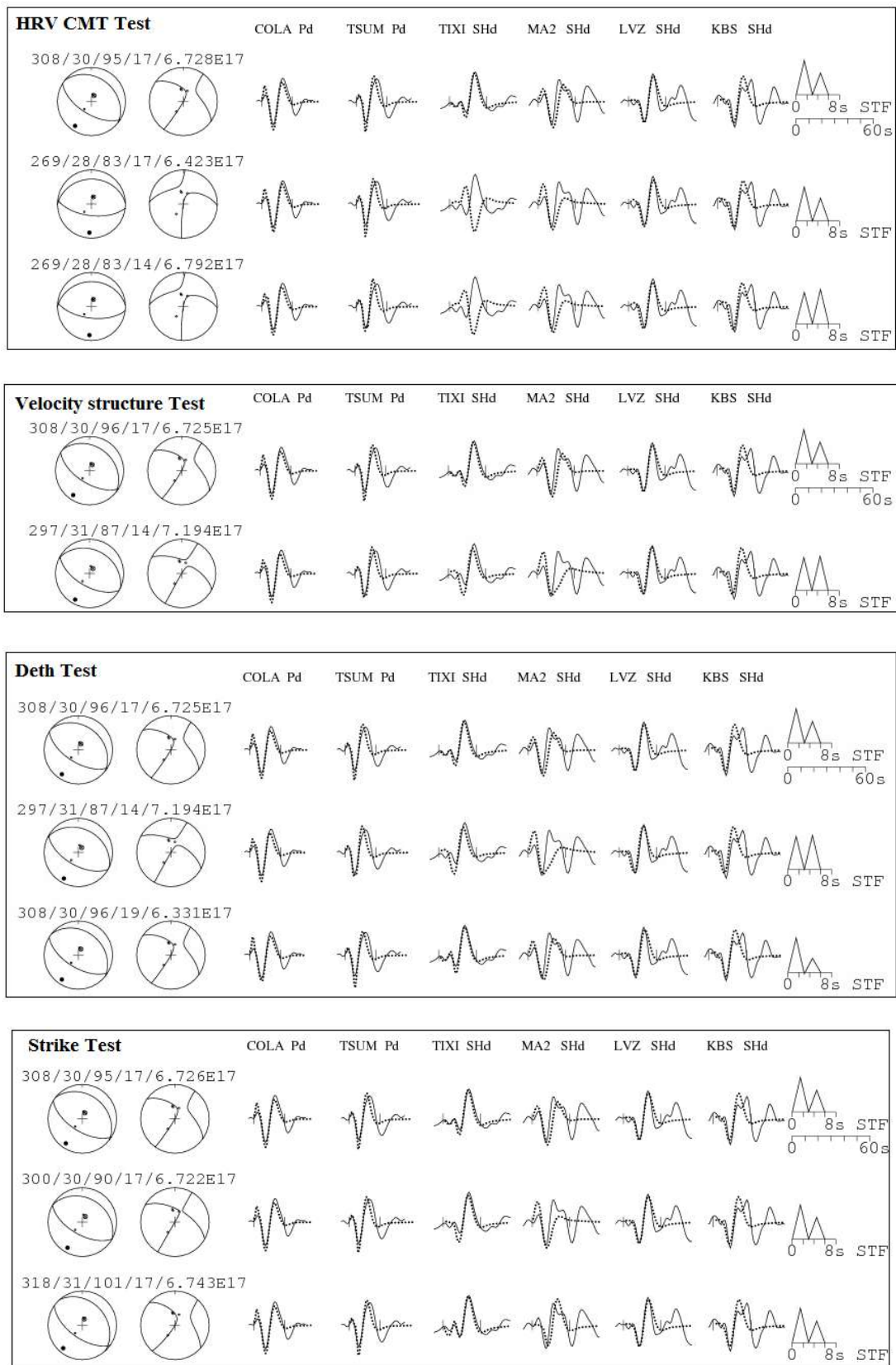


Fig. 5: Continued

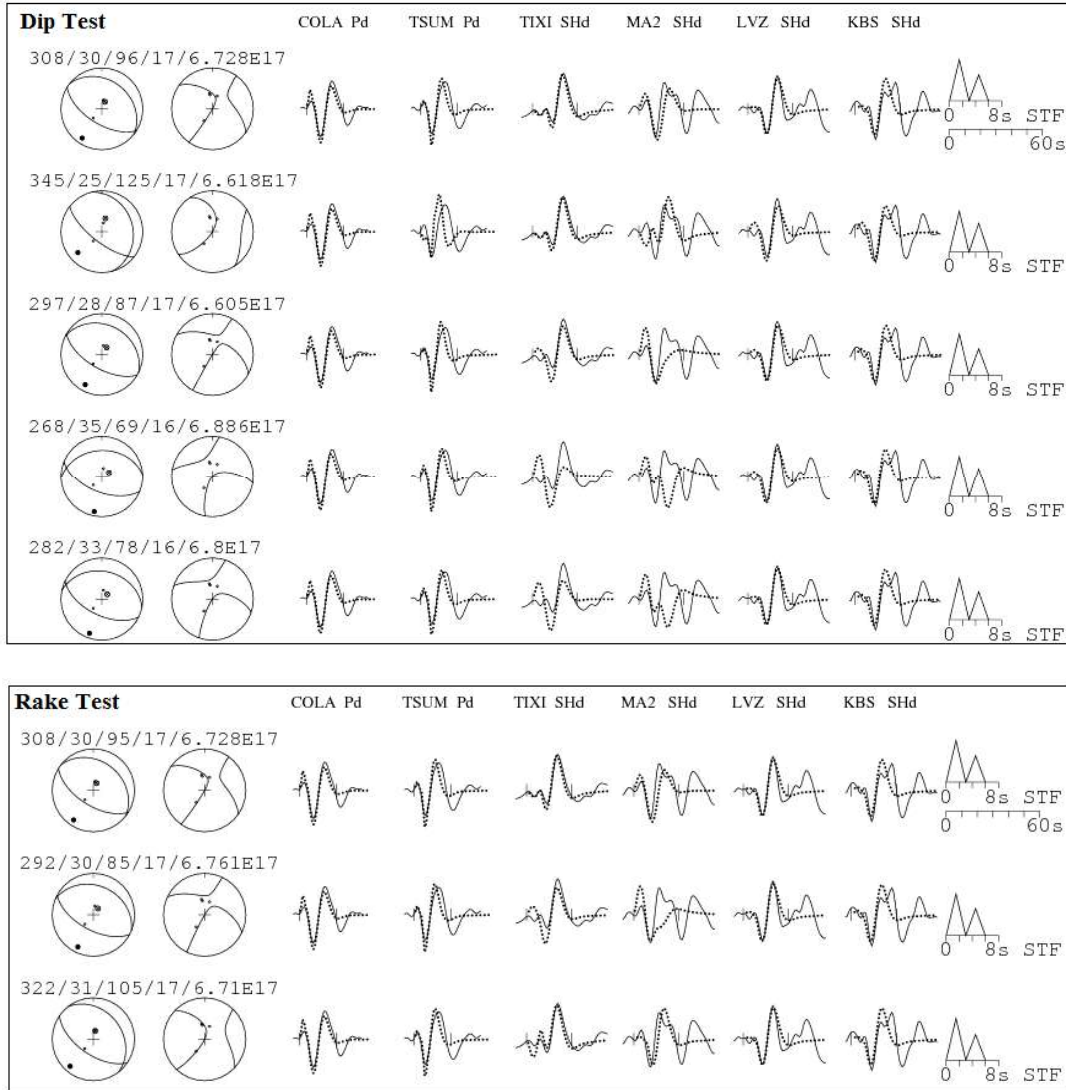


Fig. 5: Tests to check the inversion for 1998 Mach 14 earthquake (Fig. 5) for sensitivity of source parameters. Synthetic seismograms are dotted, observed as solid lines. The first line in each box shows the minimum misfit solution from Fig 4. P and SH focal spheres are shown, with the time function and numbers showing the strike, dip, rake, centroid depth and seismic moment. The first box shows the HRV CMT tests the first line in this box indicates the best fit in this study, the second line is the HRV CMT solutions with depth free and the last line shows the CMT solutions in which all parameters are fixed. The second box shows the various velocity structure, in the first line we carried out a velocity model with a single layer over a half space (see text) and in the second line a half space with  $V_p = 6.5 \text{ km.s}^{-1}$ ,  $V_s = 3.75 \text{ km s}^{-1}$  and  $\rho = 2.85 \text{ g cm}^{-3}$ . The other boxes show the depth, strike and dip tests with a single layer on a half space velocity structure

Maggi *et al.* 2000 [19], we carried out all inversions on a supposed single 10 km thick layer with  $V_p = 6 \text{ km.s}^{-1}$ ,  $V_s = 3.45 \text{ km.s}^{-1}$  and  $\rho = 2.78 \text{ gr.cm}^{-3}$  above a half space with  $V_p = 6.8 \text{ km.s}^{-1}$ ,  $V_s = 3.92 \text{ km.s}^{-1}$  and  $\rho = 2.91 \text{ gr.cm}^{-3}$ . In addition to this velocity structure model, as explained above, the realistic changes in the velocity

model make little change in orientation or depth, we carried out the inversion in a half space with  $V_p = 6.5 \text{ km.s}^{-1}$ ,  $V_s = 3.7 \text{ km.s}^{-1}$  and  $\rho = 2.85 \text{ gr.cm}^{-3}$ , then we estimated the uncertainty in moment to be  $\pm 4.44 \times 10^{16} \text{ N.m}$  or  $\sim 7$  percent. With a typical rupture velocity of  $ca 3.5 \text{ km.s}^{-1}$ , the fault length may be  $\sim 16 \text{ km}$ .

Our results are approximately in accordance with those obtained from CMT solutions but significant difference is in strike (Table 1 and first box in Fig. 5). Due to the existence of NW-SE faults in this region, we believe our model is more reliable.

### SOURCE PARAMETERS FROM FAR-FIELD DISPLACEMENT SPECTRA

**Methodology:** Source parameters such as moment ( $M_0$ ), fault length ( $L$ ), average displacement ( $u$ ) across the

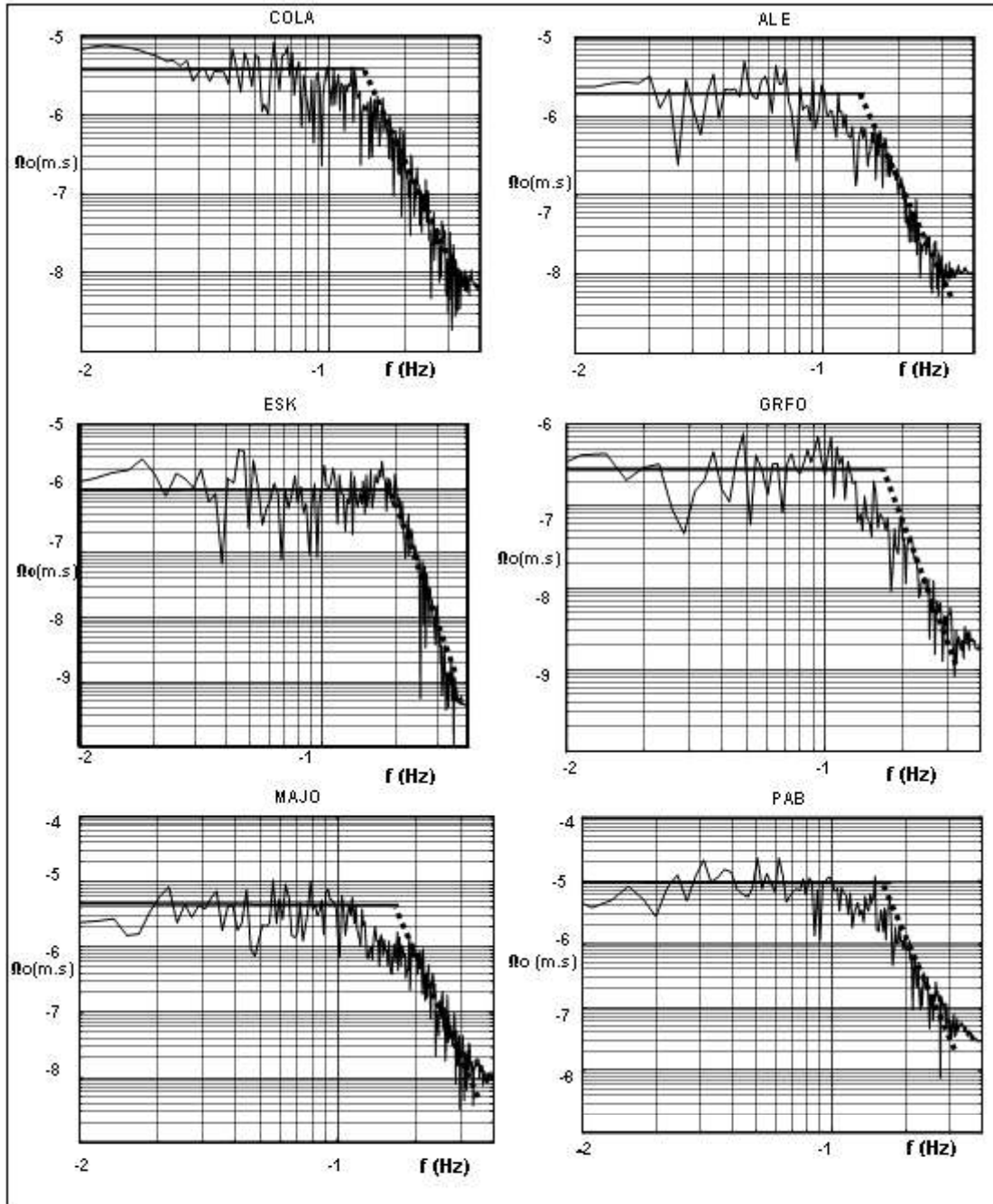


Fig. 6: Far-field amplitude displacement spectra are used to estimate the fault dimensions and other parameters of the Fandoqa mainshock. The low and high frequency asymptotes (fitted by eye) are depicted as straight lines. The corresponding values of the low-frequency part of the spectrum,  $O_0$  and the corner frequency,  $f_c$ , are also shown for each spectrum. The axes values are logarithmic

fault and static stress drop ( $\Delta\sigma$ ), were determined for the Fin mainshock, using the far-field amplitude displacement spectra. The data consist of long period  $P$ -waves with sampling frequency of 1 Hz in which are recorded at teleseismic distances ( $30^\circ$ - $90^\circ$ ) from the GSN stations. In order to include amplitudes comparable to the maximum amplitudes of the  $P$ -wave train, we used a time window starting at the  $P$ -wave arrival and ending before the  $S$ -wave arrival, therefore containing both  $P$ -wave and its coda. The displacement waveform is corrected for the instrument response, attenuation and radiation pattern. The far field amplitude displacement spectra are characterized by 3 parameters: i) the low frequency level,  $O_o$ , which is proportional to seismic moment; ii) the corner frequency,  $f_c$  and iii) the power of the high frequency asymptote. Following Brune [20, 21] we define corner frequency at the intersection of low-and high-frequency asymptotes in the spectrum.

Almost all far-field displacement spectra were characterized by a constant low-frequency level,  $O_o$  and a fall-off above a corner frequency,  $f_c$ , at a rate proportional to  $f^{-y}$ . Spectra that did not show such a shape were not analyzed. Determination of the spectral parameters ( $O_o$ ,  $f_c$ ) was performed by eye fitting low-and high-frequency asymptotes to the observed spectra. Figure 6 shows indicatively the displacement amplitude spectra for 6 stations together with their best fitting results.

The scalar seismic moment was calculated by the relation [22],

$$M_o(P) = 4\pi\rho Ra^3 [O_o(P)/R_{\theta\phi}] \quad (1)$$

where  $O_o(P)$  denotes the low-frequency asymptote of the spectrum,  $\rho$  the density at the source,  $R_{\theta\phi}$  the radiation pattern coefficient for  $P$ -waves from a double couple point source,  $R$  the epicentral distance and  $a$ , the  $P$ -wave velocity at the source.

In order to calculate the source dimensions and the stress drop, a circular fault of radius  $r$  was assumed. To estimate the fault radius, we examined four models as followed:

$$r(P) = 0.32\beta/f_{cp} \text{ Madariaga Model [23]} \quad (2)$$

$$r(P) = 0.37a/f_{cp} \text{ Brune Model [21]} \quad (3)$$

$$r(P) = 0.24 a/f_{cp} \text{ Sato and Hirasawa Model [24]} \quad (4)$$

$$r(P) = 0.1\beta/f_{cp} \text{ Bresnev Model [25]} \quad (5)$$

where  $f_{cp}$  is the corner frequency of the  $P$ -wave spectra and  $\beta$  is the velocity of shear waves. We have also

assumed that the diameter of the circular fault area is equal to the observed fault length [26].

Stress drop was calculated by the relation of Keilis-Borok relation [22],

$$\Delta\sigma = (7M_o)/16r^3 \quad (6)$$

and the average displacement,  $u$ , was calculated by the Aki relation [27],

$$M_o = \mu A u \quad (7)$$

where  $\mu$  is the shear modulus (typically  $3 \times 10^{10}$  N.m<sup>-2</sup> in the crust) and  $A$  is the fault surface.

Since the earthquake represents a release of elastic on a dislocation, the average strain, which is the ratio of average slip ( $u$ ) to fault length ( $L$ ), can be related to the change in stress ( $\Delta s$ ) on the earthquake fault through the rigidity,  $\mu$ , thus

$$\Delta\sigma = \mu u / L \quad (8)$$

The stress drop ( $\Delta\sigma$ ) was calculated for various models so as to test them with those obtained from the Aki [27] relation.

Average values  $\langle x \rangle$  were computed for each parameter (stress drop, fault length, average displacement) following Archuleta *et al.* [28],

$$\langle x \rangle = \text{anti Log} [(1/N)\Sigma \text{Log } x_i] \quad (9)$$

where  $N$  is the number of stations in use. The basic reason for using this relation is that in the case of simple arithmetic average, the mean values are biased towards the larger values. The corresponding standard deviation of the logarithm  $SD(\text{log } \langle x \rangle)$  and the multiplicative error factor,  $E_x$ , were also calculated by Archuleta *et al.* relations [28],

$$SD(\text{Log } \langle x \rangle) = [(1/N-1)\Sigma (\text{Log } x_i - \text{Log } \langle x \rangle)^2]^{1/2} \quad (10)$$

$$E_x = \text{anti Log} (SD(\text{Log } \langle x \rangle))$$

**Source parameters from the spectral analysis:** For all calculations, we used values of  $6.5 \text{ km.s}^{-1}$  and  $3.7 \text{ km.s}^{-1}$  for the  $P$ -and  $S$ -waves velocity, respectively, a density of  $2.85 \text{ gr.cm}^{-3}$  and a value of  $3 \times 10^{10} \text{ N.m}^{-2}$  for the shear modulus,  $\mu$ .

The distance, the azimuth, the take-off angle, the low frequency asymptote,  $O_o$  and the corner frequency ( $f_c$ ) of 22 stations that were used are listed in Table 2. Table 3 lists the average values and the multiplicative factor of the average of scalar seismic moment ( $M_o$ ), average radius ( $r$ ) or the half length of

Table 2: Station and spectral parameters obtained from far-field displacement spectra of P-waves for March 25, 2006 Fin earthquake. Columns show, the station code, station azimuth, take-off angle, station distance from earthquake epicenter, low-frequency asymptotes of spectrum and corner frequency, respectively

S-Code	Az (deg)	Ta (deg)	Dis (km)	Oo(m.s)	f <sub>c</sub> (Hz)
KIEV	326.0	32.3	3403	4.70E-6	0.12
OBN	338.5	32.6	3427	3.50E-6	0.15
KMBO	221.0	27.0	3735	6.00E-6	0.10
GRFO	315.0	30.3	4492	4.00E-7	0.15
CHTO	93.0	30.2	4512	4.74E-6	0.13
BFO	313.0	30.1	4660	9.00E-6	0.13
ULN	48.7	29.5	4945	9.98E-6	0.10
KEV	345.0	28.4	5043	1.10E-6	0.16
ESK	319.0	28.5	5583	1.20E-6	0.21
PAB	300.0	27.8	5626	1.00E-6	0.15
KBS	351.0	26.5	6099	6.80E-6	0.15
TATO	76.3	25.3	6498	1.10E-6	0.17
TIXI	20.8	25.2	6538	1.80E-6	0.13
INCN	60.9	25.0	6601	2.80E-6	0.12
ALE	353.0	23.0	7374	3.00E-6	0.15
SUR	211.0	22.4	7587	4.00E-6	0.16
MAJO	59.1	22.2	7620	4.80E-6	0.18
MA2	33.0	22.1	7686	9.00E-6	0.15
YSS	47.3	22.3	7617	2.50E-6	0.12
SFJD	336.5	21.7	7896	3.70E-6	0.16
MBWA	121.0	19.5	8742	6.70E-6	0.14
COLA	10.0	17.5	9568	3.40E-6	0.14

Table 3: Average values and multiplicative error factors of the fault radius, r, dislocation on fault, u, release strain, u / L, where L = 2r is the fault length and the stress drop, Δσ, which we calculated for various models are used

	r (km)	u (cm)	u/L	Δσ (bars)
Brune Model [21]	17.76 (±1.8)	2.16 (+0.45/0.36)	6.08 (+1.78/1.32)E-7	0.36 (+0.10/0.08)
Madariaga Model [23]	8.47 (±1.8)	9.50 (+4.46/2.55)	5.61 (+3.64/2.01)E-6	3.36 (+2.18/1.20)
Sato-Hirasawa Model [24]	11.5 (±1.8)	5.15 (+1.57/1.13)	2.24 (+1.02/0.65)E-6	1.34 (+0.61/0.39)
Bresnev Model [25]	2.65 (±1.8)	97.00 (+60/53)	1.83 (+2.25/1.15)E-4	109.87 (+56/75)

the fault, the stress drop (Δσ) and the average displacement across the fault, for a circular fault from various models.

The value of the scalar seismic moment based on Eq. (1), is  $6.42 \times 10^{17}$  N.m, which is accordance with that, is obtained by body waveform modeling in this study (Table 1). The statistic stress drop that was deduced from the Keilis-Borok model [22], Δσ = 2.88 bars, is closer to the value obtained from Madariga model [23] than the other models (Table 3).

By comparing the results of these four models, we observe large differences between them. For example, the Brune circular model results in a fault length of ~35.5 km (2r), considerably overestimated and the Bresnev circular model results a length of ~ 5.3 km which is underestimated as compared to the two other

models. It seems that the reliable result of the fault length, displacement and statistic stress drop in this event, is based on the Madariaga model [23], which is a good in accordance with those obtained from experimental observation in elsewhere.

## DISCUSSION AND CONCLUSIONS

We investigated the source parameters of the Fin Mw 5.8 earthquake that occurred in the southeast end of Zagros Mountains (Iran) at Hormozgan Province. We used P-and SH-waveform modeling and the spectral analysis of the far-field displacement P-wave spectra in parallel, to ensure reliable estimation of the scalar seismic moment. In this study, the results are as followed:

- Figure 4 and 5 show the focal mechanism and parameter tests of the Fin main-shock earthquake. The tests show our solutions are more reliable in compare with the HRV CMT solutions.
- The March 25, 2006 Fin earthquake parameters (using the waveform modeling) are: Fault plane (strike = 308°, dip = 30°, rake = 95°) and auxiliary plane (strike = 113°, dip = 60°, rake = 100°), depth 17 km,  $M_0 = 6.73 \times 10^{17}$  N.m and source duration of 6 s.
- The Fin earthquake was caused by a thrust motion on a hidden fault at the basement of Arabian plate.
- It seems that the NW-SE striking plane is the fault plane which implies sinisterly thrust motion contrary to what is expected from the basement motion and cluster events in a short duration at study area.
- The obtained seismic moment value from spectral analysis is close to the estimated value by waveform modeling.
- *P*-wave long period spectral analysis results, the fault length  $L \sim 17$  km which is in accordance with those deduced from rupture velocity assumption; stress drop  $\Delta\sigma \sim 2.88$  bars and average displacement  $u \sim 9.5$  cm. (Table 3).
- In order to determine the fault dimension, dislocation on fault and statistic stress drop, we tested the various circular models and found that the Madariaga Model [23] is more consistent in comparison to the other models so as to observe value elsewhere (Table 3).

#### ACKNOWLEDGMENTS

This research is related to Ph.D. project (5323 code) of the first author at International Institute of Engineering Earthquake and Seismology (IIEES). We would like to thank the IRIS team for providing the data and Harvard University for providing the CMT solutions. We thank Professor Engdahl who kindly provided us the final catalogue for events in the area of Iran. Special thanks to Professor James Jackson, Dr. Kith Priestly, Dr. Alessia Maggi, Dr. Peter Zwick and Dr. Hussein Hamzehloo for their helpful comments during this research.

#### REFERENCES

1. Tatar, M., D. Hartzfeld, J. Martinod, A. Walpersdorf, M. Ghafpri-Ashtiany and J. Chery, 2002. The present-day deformation of the central Zagros from GPS measurements, *Geophys. Res. Lett.*, 29 (19): 1927, doi: 10.1029/2002GL015427.
2. Vernant, P., F. Nilforoshan and D. Hartzfeld *et al.*, 2004a. Present-Day Crustal Deformation and Plate Kinematics in Middle East Constrained by GPS Measurements in Iran and Northern Oman. *Geophys. J. Intl.*, 157: 381-398.
3. Beydoun, Z.R., 1991. Arabian plate hydrocarbon potential-a plate tectonic approach. *AAPG Special Studies Series*, 33: 77.
4. Talebian, M. and J.A. Jackson, 2002. Offset on the Main Recent Fault of the NW Iran and implications for the late Cenozoic tectonics of the Arabian-Eurasia collision zone. *Geophys. J. Intl.*, 150: 422-439.
5. Berberian, M., 1995. Master blind thrusts faults hidden under the Zagros folds: Active basement tectonics and surface morphotectonics, *Tectonophysics*, 241: 193-224.
6. Allen, M.B., J.A. Jackson and R. Walker, 2004. Late Cenozoic reorganization of the Arabia-Eurasia collision and comparison of short-term and long-term deformation rates, *Tectonics*, 23 TC2008, doi: 10.1029/2003TC001530.
7. Jackson, J.A., 1980. Reactivation of basement faults and crustal shortening in organic belts. *Nature*, 283: 343-346.
8. Jackson, J.A. and T.J. Fitch, 1981. Basement faulting and the focal depths of the larger earthquakes in the Zagros Mountains (Iran), *Geophys. J. R. Aster Soc.*, 64: 561-585.
9. Belance, E.J.-P., M.B. Allen, S. Inger and H. Hassani, 2003. Structural styles in the Zagros Simple Folded Zone. *Iran, J. geol. Soc. Lond.*, 160: 401-412.
10. Ambraseys, N.N. and C.P. Melville, 1982. *A History of Persian Earthquakes*, Cambridge University Press.
11. Nábélek, J., 1984. Determination of earthquake source parameters from inversion of body waves. PhD Thesis, Massachusetts Institute of Technology.
12. McCaffery, R., P. Zwick and G. Abers, 1991. SYN 4 Program, IASPEI Software Library, 3: 81-166.
13. Zwick, P., R. McCaffery and G. Abers, 1994. MT5 program, IASPEI Software Library.
14. McCaffery, R. and G. Abers, 1988. SYN3: A program for inversion of teleseismic body waveforms on microcomputers. *Air Force Geophys. Lab. Tech. Rept*, AFGL-TR-88-0099, Hanscomb Air Force Base, Ma.
15. Langston, C. and D.V. Helmberger, 1975. A procedure for modeling shallow dislocation sources, *Geophysics. J. R. Astorn. Soc.*, 42: 117-130.
16. Futterman, W., 1962. Dispersive body waves, *J. geophys. Res.*, 67: 5279-5291.

17. McCaffery, R. and J. Nabelek, 1987. Earthquakes, gravity and the origin of the Bali basin: An example of a nascent continental fold-and-thrust belt. *J. geophys. Res.*, 92: 441-460.
18. Molnar, P. and H. Lyon-Cean, 1989. Fault plane solutions of earthquakes and active tectonics of Tibetan Plateau and its margin, *Geophys. J. Intl.*, 99: 123-153
19. Maggi, A., J.A. Jackson, K. Priestley and C. Baker, 2000. A re-assessment of focal depth distribution in southern Iran, the Tien Shen and northern India: Do earthquakes really occur in continental mantle? *Geophys. J. Int.*, 143: 629-661.
20. Brune, J.N., 1970. Tectonic stress and the spectra of seismic shear waves from earthquakes. *J. Geophys. Res.*, 75: 4997-5009.
21. Brune, J.N., 1971. Correction (to Brune, 1970), *J. Geophys. Res.*, 76: 5002.
22. Keilis-Borok, V.I., 1959. On the estimation of the displacement in an earthquake source and source dimensions. *Ann. Geofis.*, 12: 205-214.
23. Madariaga, R., 1976. Dynamics of the expanding circular fault, *Bull. Seismol. Soc. Am.*, 66: 639-666.
24. Sato, T. and T. Hirasawa, 1973. Body wave spectra from propagating shear cracks. *J. Physics of the Earth*, 21: 415-431.
25. Beresnev, A., 2002. Source Parameters Observable from Corner Frequency of Earthquake Spectra. *Bulletin of the Seismological Society of America*, 92 (5): 2047-2048.
26. Hanks, T.C. and M. Wyss, 1972. The use of body-wave spectra in the determination of seismic-source parameters. *Bull. Seismol. Soc. Am.*, 62: 561-589.
27. Aki, K. 1966: Generation and propagation of G waves from the Niigata earthquake of June 16, 1964. Part 2. Estimation of earthquake moment, released energy and stress-strain drop from the G-waves spectrum, *Bull. Earthquake Res. Ins., Tokyo Univ.*, 44, 73-88.
28. Archuleta, R.J., E. Cranswinck, C.H. Mueller and P. Spudich, 1982. Source parameters of the 1980 Mammoth lakes. California, Earthquake Sequence, *J. Geophys. Res.*, 87: 4595-4607.